

The visco-damage mechanical response of swirl-mat composites

L.V. SMITH¹ and Y.J. WEITSMAN²

¹*The University of Tennessee Knoxville, TN, U.S.A.*

²*Mechanical and Aerospace Engineering and Engineering Science, University of Tennessee, 307 Perkins Hall, Knoxville, U.S.A. e-mail: weitsman@utk.edu*

Received 24 March 1997; accepted in revised form 13 November 1997

Abstract. This article concerns the characterization of the mechanical response of composite materials made of continuous, randomly oriented strands ('swirl-mat') of E-glass fibers embedded in a urethane matrix. The purpose of this work is to identify and quantify the various parameters that govern the material response in order to develop a predictive model. The characterization is based upon creep data collected during the application of constant load of several amplitudes and various durations, and recovery data collected after load release. The glass-fiber/urethane matrix swirl-mat composites were observed to develop distributed damage in the form of profuse internal micro-cracks, they exhibit time-dependent response and develop permanent deformation upon load removal. A one dimensional model is presented, which incorporates the foregoing features of creep, continuum damage, and permanent deformation. The model is employed to represent the characterization data as well as to predict the response under two-step load histories.

Key words: Random polymeric composites, damage, creep, non-linear response.

1. Introduction

This article presents an experimental investigation of the mechanical response of swirl-mat E-glass fiber/urethane matrix composites. Such composites are being considered as candidate materials in the automotive industry due to their relatively low costs and their amenability to rapid and versatile manufacturing. The purpose of this study is to identify the various mechanisms that occur in those composites under load and quantify their effects on the mechanical response.

Swirl-mat composites consist of a 'dry' fiber preform, shown in Figure 1, and a polymeric matrix that serves as a binder. The swirl-mat preform is produced by placing continuous E-glass fiber strands onto a moving conveyor in random circular patterns. A polymeric coating is applied to the mat to fix its shape and enhance wettability during the subsequent processing stage. That stage consists of a rapid injection of urethane resin by a SRIM (structural reaction injection molding) process. This process, which is completed within a very short time, is deemed to be highly cost effective. On the other hand, the rapidity of the above process results in non-uniformly distributed resin and an estimated void content $V_v \sim 5$ percent. Typically the fiber content is ~ 45 percent by weight, or $V_f \sim 32$ percent by volume. The foregoing non-uniformity, when compounded with the randomness in fiber orientation shown in Figure 1, yields a scatter of about 20 percent in material properties. This scatter tends to overshadow the effects of the several mechanisms that govern the material's response and must be treated by an appropriate scaling method in order to develop a rational constitutive model.

Experiments were performed with test coupons of dimensions $200 \times 25 \times 3$ mm ($8 \times 1 \times 0.125$ in.). The thickness of 3 mm (0.125 in.) corresponds to a lay-up of five swirl-mat layers, but there was no evidence of delamination throughout the test program. The

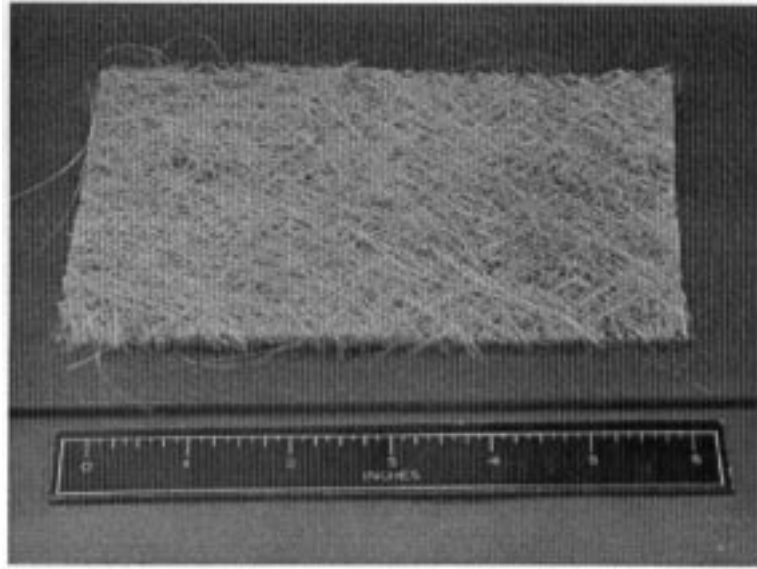


Figure 1. Photograph of a section of a continuous strand swirl-mat preform.

coupons were cut from flat plaques of dimensions $635 \times 635 \times 3$ mm ($25 \times 25 \times 0.125$ in.) that were provided by the Automotive Composites Consortium (ACC). These coupons had, on the average, a strength of 138 MPa (20 ksi), a modulus of 9.8 GPa (1.4 Msi) and a Poisson's ratio of 0.31.

Rather limited information exists at the present time regarding the response of swirl-mat composites (Tomkinson-Walles, 1988 to Corum, 1995).

As will be shown subsequently, these materials exhibit creep under all stress levels, which is commensurate with viscoelastic behavior. However, the swirl-mat composites considered in this study also show the presence of profuse microcracking under increasing loads, with the accompanying reductions in stiffness. This phenomenon may be modeled by means of continuum damage theory. Finally, these materials retain permanent, non-recoverable deformations upon load removal, a response that is akin to plastic or visco-plastic behavior.

The constitutive modeling of the foregoing 'visco-damage' response, which is motivated by the experimental data reported herein, is presented in a companion article (Abdel-Tawab and Weitsman, 1998).

Two kinds of experimental information will be presented in the sequel. The first kind, of qualitative nature, consists of various types of microscopic and NDE observations that corroborate the presence of distributed damage and illuminate several of its aspects. The second kind of data derives from an extensive program of mechanical tests. These tests consisted of the application and removal of step loads of various amplitudes and the recording of creep and recovery strains.

2. Qualitative experimental investigations

These investigations consisted of microscopic observations and employed various NDE techniques. A typical pair of ultrasonic *c*-scan images of a failed and virgin coupon is presented in Figure 2. (The failure surface is on the top edge of the left image.) A comparison of these

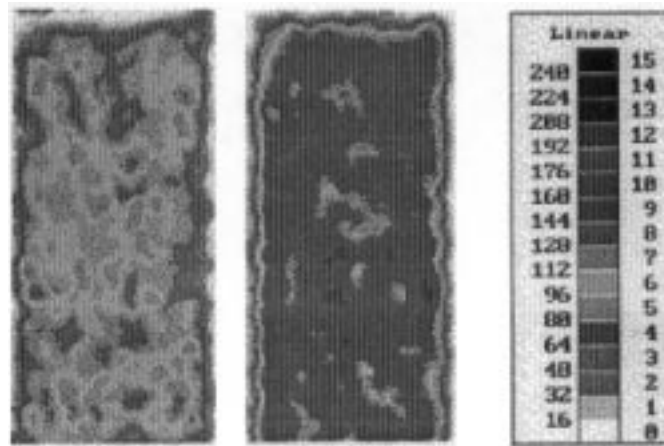


Figure 2. Ultrasonic *c*-scan images of swirl-mat coupons: failed (left) and virgin (right).

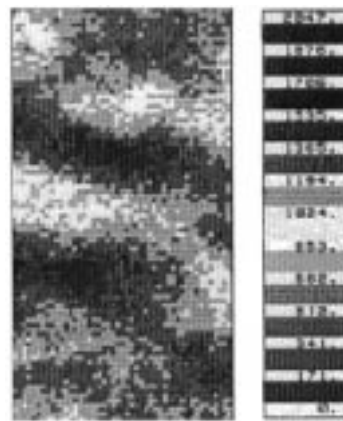


Figure 3. SPATE image (stress pattern analysis from thermal emission) of a coupon loaded to 50 percent UTS.

images indicates that damage is not localized near the fracture surface. Similar changes have been observed in coupons loaded to intermediate stress levels, below failure, showing that load affects the material in a distributed, rather than localized manner.

The thermal emission of a coupon statically loaded to 50 percent of its UTS (ultimate tensile strength) has been observed using SPATE (stress pattern analysis from thermal emission), as shown in Figure 3. This image demonstrated that damage is distributed throughout the coupon. Nevertheless, this image exhibits a periodicity which can be correlated with the spatial variations in fiber concentration in the preform.

Four kinds of microscopic techniques to observe damage will be noted herein. The first kind, which was the only method that enabled in-situ observation of damage growth, took advantage of the translucency of the material by shining a light through the back of the coupon and focusing a video microscope on regions within the material from the front side. Video images were recorded for specimens stressed within a load frame. Figure 4 shows images taken just before and after the formation of a micro-crack, with ellipses enclosing the region of microscopic observation. In general, micro-cracks tended to grow within fiber strands in regions with pre-existing defects and most commonly at orientations normal to the direction

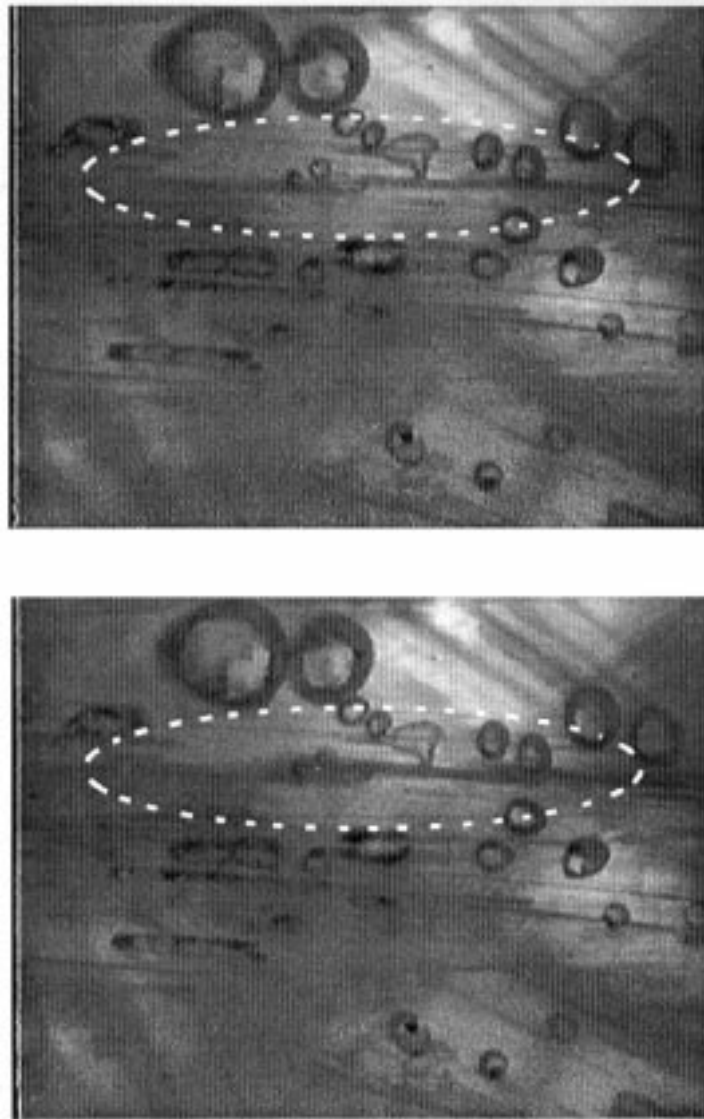


Figure 4. Optical microscopy of a microcrack: before damage (top) and after damage (bottom). Horizontal field of view is approximately 1.3 mm (0.05 in.).

of load. The location and orientation of the cracks suggest that damage is largely a result of a weak fiber/matrix interface. This may be due to inadequate fiber/matrix adhesion, poor wetting of fiber strands, or thermal or curing induced mismatched shrinkage.

The latter conclusion is supported by SEM observations of fractured surfaces exhibited in Figure 5. This micrograph shows separations between individual fibers within a fiber strand and 'river patterns' within the resin that emanate from interfaces between the polymer and fiber strands. These patterns suggest crack initiation at those interfaces. While observations of this nature may appear preliminary at this point, they are nevertheless in agreement with ongoing investigations (Herring, 1997).

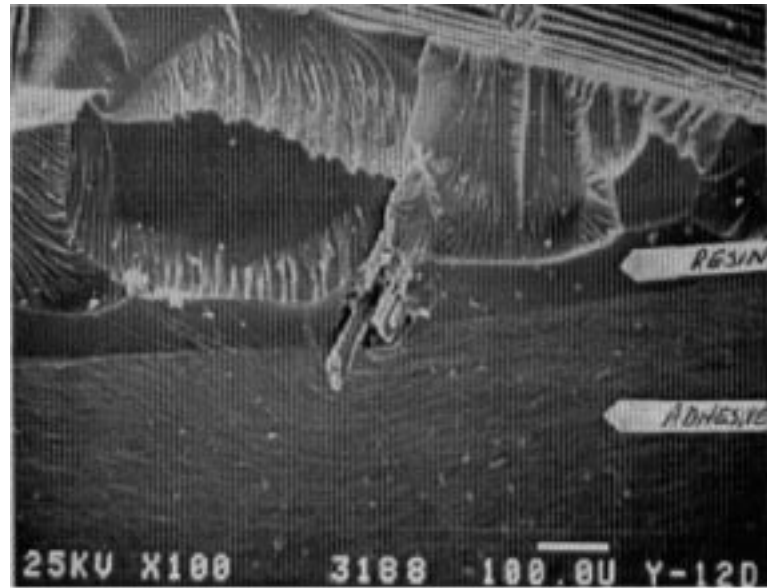


Figure 5. Scanning electron beam microscope image of a fracture surface. 'River patterns' in the matrix indicate that failure initiated at the extruding fiber strand. Note also the gaps between the fibers within the strand directed downward.

Images of two coupons taken using a confocal laser scan microscope are presented in Figure 6. (The top image is from an unloaded coupon, the bottom image is from a coupon that was previously loaded to 60 percent UTS for one week.) While the size and density of micro-cracks is clearly lower for the unloaded coupon, Figure 6 shows that the virgin material contains a multitude of initial flaws.

An unloaded crack, grown from an edge notched coupon, is presented in Figure 7. Note that the opposing crack faces did not close completely upon load removal due to the roughness of their surfaces. This suggests that permanent deformation may not be associated with plasticity in the classical sense, but is more appropriately attributable to the roughness of crack surfaces, which in turn is related to the random fiber architecture.

3. Quantitative characterization experiments

These tests consisted of the single application of step stresses of several amplitudes σ_0 and their removal after various durations t_0 , as shown in Figure 8(a). Creep and recovery strains, as sketched in Figure 8(b), were recorded in association with the above stresses. A summary of the experiments included in the test program is given in Table 1, below.

Recovery data were collected for durations $t_r \geq 3t_0$ after load removal. All experiments were performed on a four post, 44 kN (20 kip) MTS hydraulic load frame. Strains were measured by means of foil resistance gages bonded to the specimen surface. Care was taken to minimize strain measurement error given the long creep durations and small recovery strains. An estimate of the effects of fluctuations in the laboratory environment on the specimens' strain was obtained through the simultaneous recording of strains in a control specimen that was not subjected to mechanical loads. Strain signals were converted to voltages using Vishay

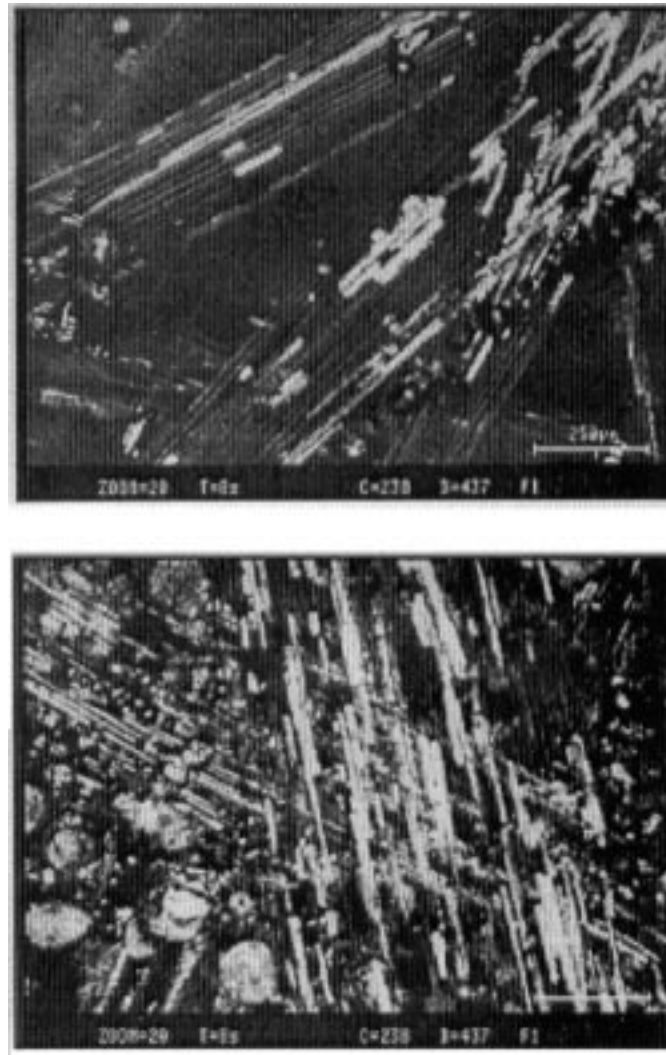


Figure 6. Confocal laser scan images of swirl-mat coupons: virgin (top) and after 7 days at 83 MPa (12 ksi) (bottom).

2310 conditioners, digitized with the load signal using an HP 3852 Data Acquisition Control Unit and stored on a computer using LabView.

It should be noted that loading and unloading could not be realized in the step fashion shown in Figure 8(a). In reality, loading and unloading were applied at a constant rate, requiring between 5 to 15 seconds to attain prescribed levels.

The first step in the characterization program consisted of identifying the range of linear response, where the creep strain $\varepsilon(t)$ is proportional to σ_0 , with complete recovery upon load removal, i.e. $\varepsilon_r(t) \rightarrow 0$ as $t \rightarrow \infty$. This range was determined experimentally to occur when the applied stresses were below the threshold value of $\sigma_d \approx 36$ MPa (5.2 ksi). Within the foregoing range the loading and unloading compliances were of equal magnitudes, indicating the absence of damage-induced softening. Following established procedures (Jerina et al.,

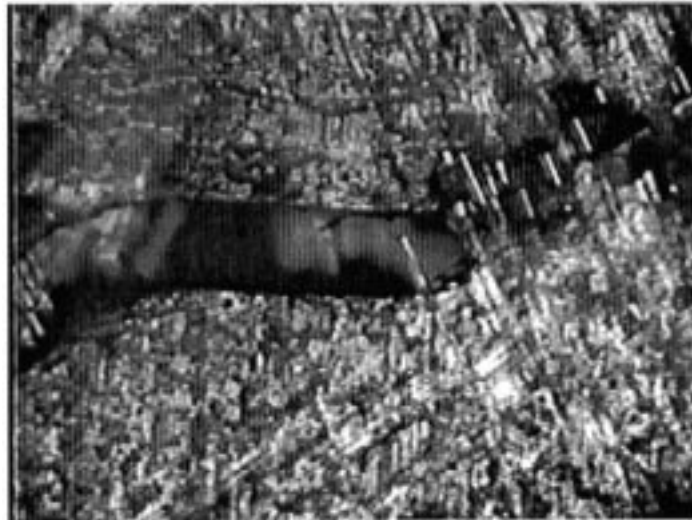


Figure 7. Surface crack from an edge notch coupon, after load removal. (Note non-closing crack faces).

Table 1. The mechanical characterization test program. Entries within the table indicate the number of replicate coupons.

t_0 (min.)	σ_0 MPa (ksi)								
	14 (2)	28 (4)	41 (6)	55 (8)	69 (10)	83 (12)	96 (14)	110 (16)	124 (18)
1									2
10		1	2	2	2	1	1		1
30	1	3	3	2	3	2	2	1	
100		1	2	1	1	1	1		
1,000		1	3	1	2	2	1		
10,000	1	3	1	2	2	2	2		

1982; Peretz and Weitsman, 1982) it was possible to express the creep and recovery data within the linear range in power-law form as follows

$$\varepsilon(t) = \begin{cases} (D_0 + D_1 t^n) \sigma_0 & 0 < t < t_0 \\ D_1 [t^n - (t - t_0)^n] \sigma_0 & t > t_0 \end{cases} \quad \sigma_0 \leq \sigma_d. \quad (1)$$

In Equation (1) D_0 , D_1 and n are material parameters, σ_0 is the creep stress, and t_0 signifies its duration. Since D_0 does not appear in the expression for recovery ($t > t_0$), D_1 and n are determined from the recovery data. D_0 may then be found by fitting the creep data for $0 < t < t_0$. A comparison of Equation (1) with experimental data in the linear range is presented in Figure 9. For the current material, under ambient laboratory conditions, we have $8.4 \times 10^{-11} \text{ Pa}^{-1}$ ($5.8 \times 10^{-7} \text{ psi}^{-1}$) $< D_0 < 11 \times 10^{-11} \text{ Pa}^{-1}$ ($7.4 \times 10^{-7} \text{ psi}^{-1}$), 1.1×10^{-11} (7.7×10^{-8}) $< D_1 < 2.0 \times 10^{-11}$ (1.4×10^{-7}), $0.05 < n < 0.08$, and time t in minutes*. Note

* The expressions in Equation (1) correspond to the step load history shown in Figure 8(a). However, since in reality the loads were applied and removed over short, yet finite, durations it was necessary to perform a convolution integration to determine D_0 .

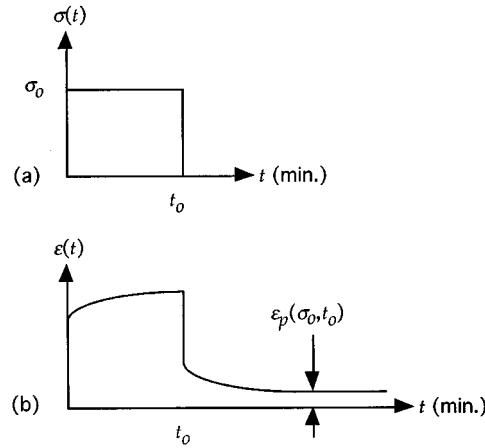


Figure 8. Schematic of stress input for a creep test (a) and the associated strain response (b).

the relatively wide range of scatter due to the inhomogeneity and randomness of the swirl-mat material. A variability of about 20 percent is most likely attributable to sample-to-sample variations in fiber orientations, volume contents of fiber, resin and voids as well as curing histories. *The foregoing wide range of scatter indicates that for the construction of a non-linear constitutive model it is necessary to scale out the variability from deformation data in the non-linear range.* Such scaling removes the major portion of the data scatter, which is due to macro-level material inhomogeneity, and enables the establishment of a rational data base and its association with a constitutive model grounded on basic principles (Abdel-Tawab and Weitsman, 1998).

A monotonic increase in compliance (modulus softening) with stress σ_0 was noted for $\sigma_0 > \sigma_d$. Such an increase is consistent with the proliferation of internal microcracks, as shown in Figures 4–7, and its modeling is accommodated by continuum damage theory.

The phenomenon of modulus softening can also be detected through quasi-static, constant rate, loading and unloading experiments as shown in Figure 10.

The increased, or ‘damaged’ compliance D_d was evaluated during load removal as the inverse chord modulus between some two intermediate stress levels. In general, the upper and lower stress levels depend on the rate of unloading and their specific values may be determined only after some trial and error. Reasonable values are those that yield consistent trends and the smoothest variation with loading parameters. In the current work these values were chosen to be 15 percent and 85 percent of the creep stress, as suggested for elastic materials (Lemaitre and Chaboche, 1990). For the rapid unloading employed in the characterization scheme, the actual values for D_d varied only slightly for intermediate values that fell within the above range. This unloading compliance, denoted by D_d , was normalized with the initial compliance, D_0 , obtained during the application of load in the stress range $0 < \sigma(t) < \sigma_d$, both of which are represented in Figure 10. The ratio D_d/D_0 is plotted in Figure 11 vs. the creep stress σ_0 . As expected, below σ_d the compliance does not vary with stress and is insensitive to its level. However, above σ_d , Figure 11 suggests that the compliance scales linearly with stress, or

$$\frac{D_d}{D_0} = K_T(\sigma) = 1 + K_d(\sigma_0 - \sigma_d)H(\sigma_0 - \sigma_d), \quad (2)$$

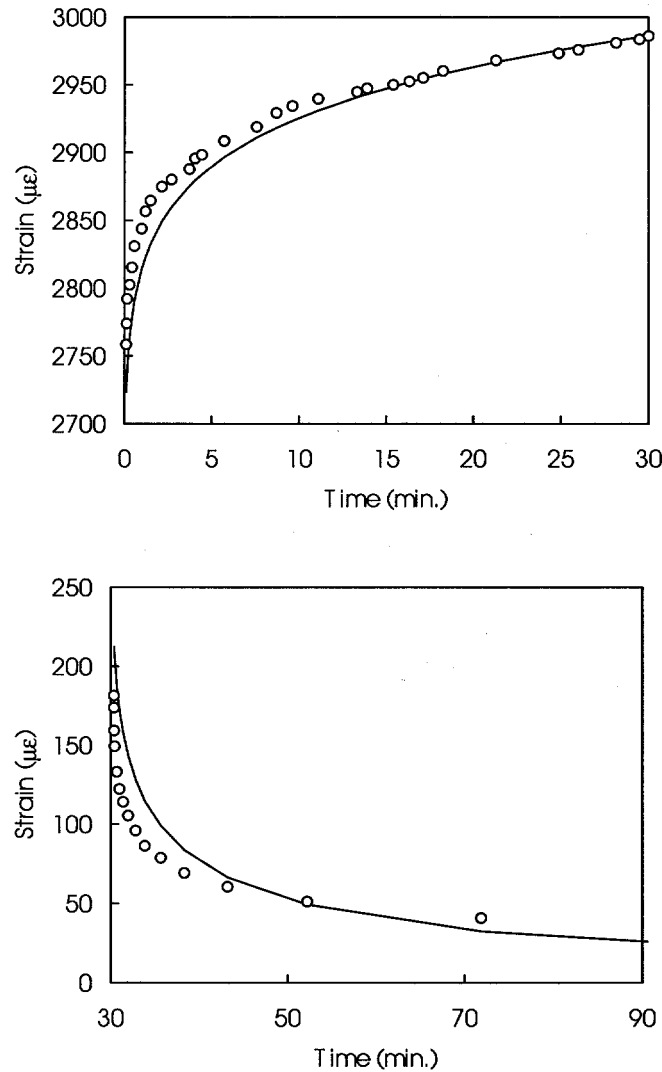


Figure 9. Comparison between the linear prediction (—) and experiment (\circ) $\{\sigma_0 = 28 \text{ MPa (4 ksi)}\}$ for creep (top) and recovery (bottom).

where $\sigma_d \approx 36 \text{ MPa (5.2 ksi)}$, $K_d = 0.0035 \text{ MPa}^{-1} (0.024 \text{ ksi}^{-1})$, and $H(\cdot)$ is the unit step function. Obviously, the foregoing values represent average quantities and do not account for the observed data scatter.

It is worth noting that a plot of the un-normalized compliance D_d vs. σ_0 fails to exhibit a consistent trend due to the aforementioned sample-to-sample variation in D_0 . This is shown in Figure 12.

Turning to the effect of damage on creep it is reasonable to expect that $D = D(\omega)$, where D is compliance and ω denotes damage associated with continuously distributed microcracks. Obviously D increases with ω , while in general $\omega = f(\sigma, t)$, growing monotonically with both stress and time.

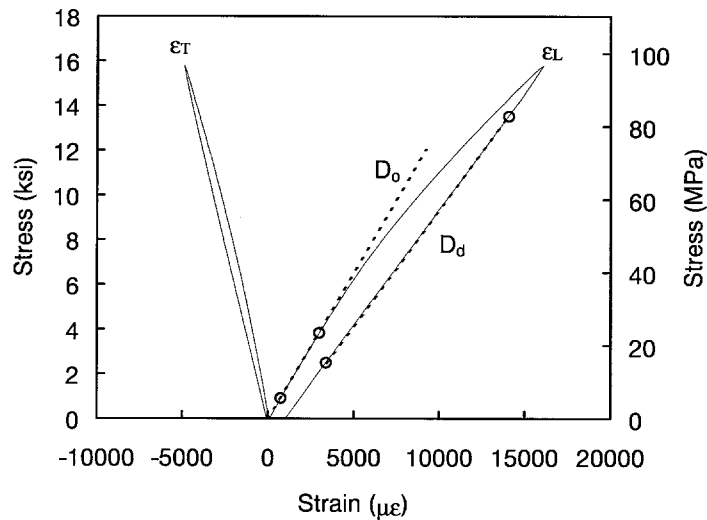


Figure 10. Longitudinal (ϵ_L) and transverse (ϵ_T) strain response of a coupon quasi-statically loaded to 80 percent UTS and then immediately unloaded. Solid lines represent experimental data, dashed lines represent compliances measured between the points indicated by open circles.

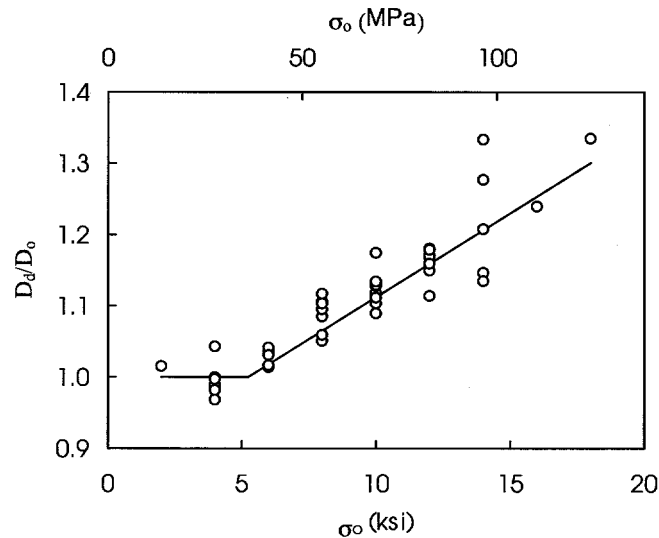


Figure 11. The effect of creep stress σ_0 on the normalized instantaneous compliance, as given by the ratio D_d/D_0 , where D_d is the damaged compliance evaluated during unloading.

The above considerations are consistent with the observation that D_d/D_0 increases monotonically with σ_0 , as shown in Figure 11 and expressed in Equation (2). One may view expression (2) as the compounded consequence of $K_T = \hat{K}_T(\omega)$ and $\omega = \hat{f}(\sigma)$.

Perhaps the most interesting observation noted during the experimental program is that the factor $K_T = K_T(\sigma_0)$ amplifies not only the instantaneous strain but scales creep strain recorded during $0 < t < t_0$. This is exhibited in Figure 13 for four randomly selected coupons, one coupon per each stress level of $\sigma_0 > \sigma_d$. The larger departure between data and prediction, which occurs at $\sigma = 96$ MPa is commensurate with the larger scatter observed at that stress

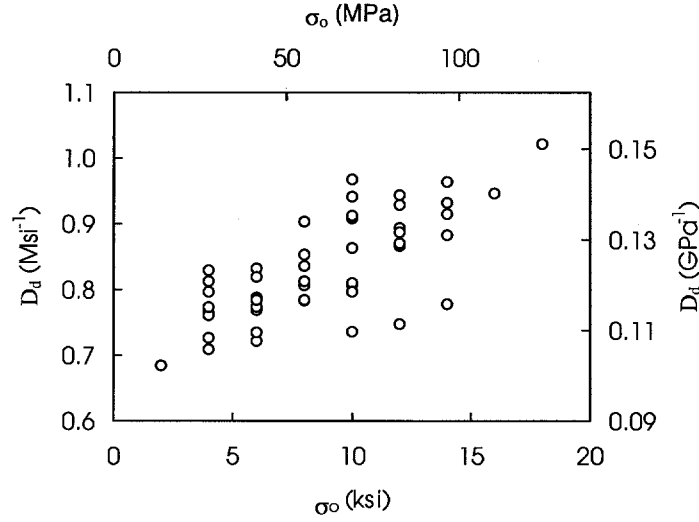


Figure 12. The effect of creep stress σ_0 on the un-normalized instantaneous unloading compliance D_d .

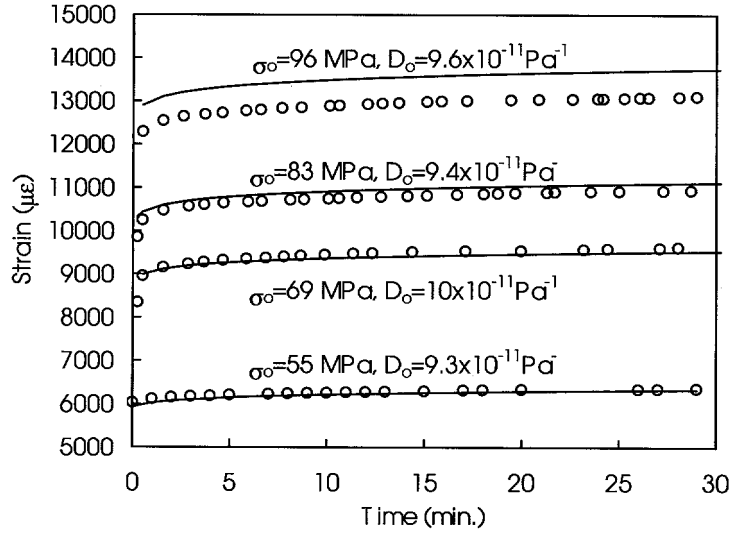


Figure 13. A comparison between the recorded (\circ) and predicted (—) creep strain for four levels of applied stress. The predicted values were obtained by employing the enhancement factor, K_T , or $\varepsilon_T(t) = K_T(\sigma)\varepsilon(t)$, where $D_1 = 2.0 \times 10^{-11}$, $n = 0.08$ and D_0 is as indicated in the figure. Recorded values correspond to single coupons, selected at random, at each stress level.

level, as noted in Figure 11. This would suggest that, *at least for the load durations employed in the present testing program*, all damage was caused rather instantaneously, with no further extension in micro-crack lengths under constantly maintained loads.

Accordingly, the total creep strain $\varepsilon_T(t)$ is given by

$$\varepsilon_T(t) = K_T(\sigma_0)(D_0 + D_1 t^n)\sigma_0. \quad (3)$$

It should be noted that in the presence of growing damage, namely $\omega = f(\sigma, t)$, the scaling expressed in Equation (3) will no longer apply and ε_T will be affected by two time scales,

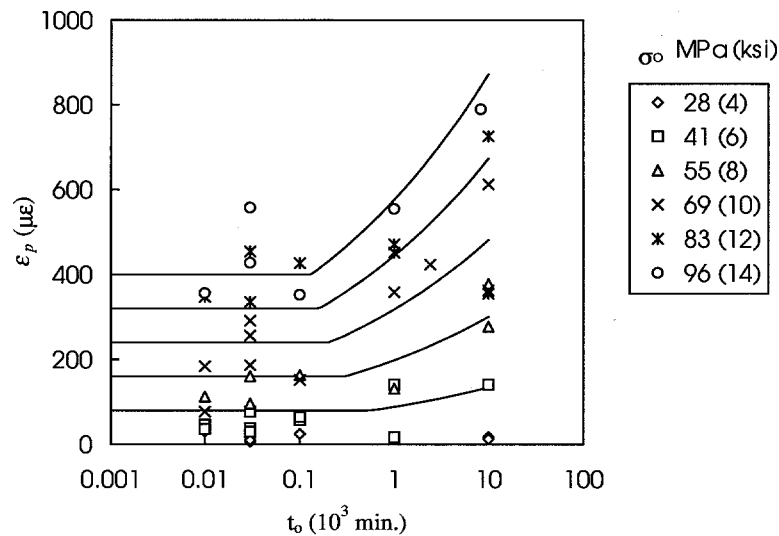


Figure 14. The effect of creep stress σ_0 and load duration t_0 on the permanent strain ϵ_p reduced at times $3t_0$ after load removal. (t_0 in 10^3 min., ϵ_p in $\mu\epsilon$).

the one due to creep and the other caused by growing damage. This circumstance, which was not encountered in the current test program, may account for the transition from secondary to tertiary creep (Abdel-Tawab and Weitsman, 1998).

Another aspect of the mechanical response of swirl-mat composites concerns the presence of permanent residual strain ϵ_p upon load removal. Unlike the circumstance of viscoelastic response, where the recovery strain ϵ_r vanishes after a sufficiently long time ($\lim_{t \rightarrow \infty} \epsilon_r(t) = 0$), the above strain ϵ_p persists even after indefinitely long times beyond load removal. Experimental observations corresponding to the test program listed in Table 1 indicate that ϵ_p depends on both stress level σ_0 and load duration t_0 . These observations also suggest that $\epsilon_p \approx 0$ for $\epsilon_{\max} < \epsilon_d$, where ϵ_d is a threshold strain analogous to σ_d .

The experimental determination of ϵ_p required the monitoring of strains in unloaded specimens for exceedingly long times. These times could extend for several weeks for load durations of $t_0 = 10^4$ minutes. In order to contain the experimental program to within a manageable time frame the recovery strains were recorded during unloading times of $t_r = 3t_0$, and the discrepancy between the measured values and those predicted by viscoelasticity were denoted by ϵ_p . Similar values of ϵ_p were obtained in the several recovery tests which extended to $t_r = 10t_0$ but somewhat lower values of ϵ_p corresponded to more prolonged durations of t_r .

Data of ϵ_p vs. load duration t_0 at various levels of σ_0 are shown in Figure 14, with curves that correspond to the best least-square fits. As can be noted from the above figure the data exhibit a wide scatter, resulting in rather poor fits.

The scatter in Figure 14 can be attributed to two major causes. First and foremost, the above data were not scaled by the initial compliance D_0 and therefore incorporate the scatter due to macro-level, sample-to-sample variability. Furthermore, as suggested by Figures 5–7, the permanent strain is caused by the roughness of the microcrack surfaces, which prevents their smooth closure upon load removal. It is intuitively clear that this roughness is inherently stochastic in nature, which would contribute to the scatter in values of ϵ_p .

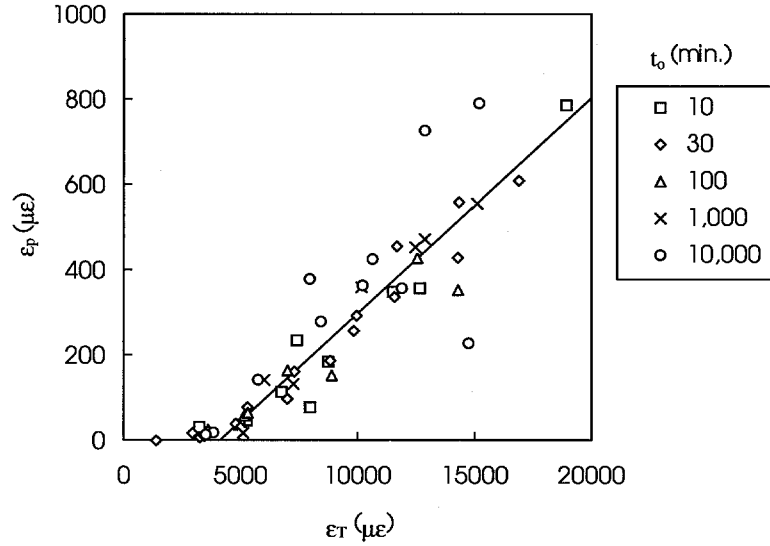


Figure 15. Dependence of permanent strain on the maximum strain.

A substantially improved correlation for ε_p is obtained when it is associated with the maximal strain ε_{\max} attained during the loading stage. Obviously, $\varepsilon_{\max} = \varepsilon_T(t_0^-)$ depends on both σ_0 and t_0 and a plot of ε_p vs. ε_{\max} would eliminate much of the scatter due to sample-to-sample variation in compliance.

The results are shown in Figure 15*. These results, which exhibit a clearer trend and much less scatter than depicted in Figure 14, can be fitted by the linear relation

$$\varepsilon_p = K_p(\varepsilon_{\max} - \varepsilon)H(\varepsilon_{\max} - \varepsilon_d). \quad (4)$$

In Equation (4) $\varepsilon_{\max} = \varepsilon_T(t_0^-)$ as evaluated from Equation (3), $K_p = 0.051$, and $\varepsilon_d = 4100\mu\varepsilon$. (The above values represent averages and do not account for data scatter.)

Note that ε_p depends implicitly on σ_0 and t_0 through ε_{\max} , incorporating the effects of damage. Although not proven conclusively here, the correlation between ε_p and ε_{\max} suggest that *expression (4) can be viewed as applicable to all stress levels and load durations σ and t , not merely for step load histories*. This hypothesis has been confirmed in a subsequent work involving cyclic loading (Smith and Weitsman, 1998). The average value of ε_d corresponds to a stress of about 44 MPa (6.4 ksi), which exceeds the threshold value of $\sigma_d \approx 36$ MPa (5.2 ksi).

Upon accounting for ε_p in accordance with Equation (4) it is possible to split the total creep strain $\varepsilon_T(t)$ into viscoelastic and permanent portions, namely

$$\varepsilon_T(t) = \varepsilon_v(t) + \varepsilon_p(t), \quad (5)$$

* Increased scatter of ε_p was observed for long duration tests ($t_0 = 10,000$ min). This may be attributed to fluctuations in laboratory humidity and temperature, which would obviously be larger for longer duration tests. Such fluctuations affect material response as well as the accuracy of electronic strain measurements.

where $\varepsilon_v(t)$ accounts for the portion of $\varepsilon_T(t)$ that will recover completely upon total unloading. Thus, if unloading occurs at $t = t_0$, we have

$$\varepsilon(t) = \begin{cases} \varepsilon_T(t) = \varepsilon_v(t) + \varepsilon_p(t) & 0 \leq t < t_0 \\ \varepsilon_r(t) = \varepsilon_v(t) - \varepsilon_v(t - t_0) + \varepsilon_p(t_0) & t > t_0. \end{cases} \quad (6)$$

Obviously, $\varepsilon_v(t) = \varepsilon_T(t) - \varepsilon_p(t)$, whereby, in view of Equation (4)

$$\varepsilon_v(t) = \begin{cases} \varepsilon_T(t) & 0 \leq \varepsilon_T < \varepsilon_d \\ (1 - K_p)\varepsilon_T(t) + K_p\varepsilon_d & \varepsilon_T \geq \varepsilon_d. \end{cases} \quad (7)$$

For the circumstance of step-load histories shown in Figure 8(a) the stress-level σ_0 may be introduced as an auxiliary parameter in Equations (6), namely

$$\varepsilon(\sigma_0, t) = \begin{cases} \varepsilon_T(\sigma_0, t) = \varepsilon_v(\sigma_0, t) + \varepsilon_p(\sigma_0, t) & 0 \leq t < t_0 \\ \varepsilon_r(\sigma_0, t) = \varepsilon_v(\sigma_0, t) - \varepsilon_v(\sigma_0, t - t_0) + \varepsilon_p(\sigma_0, t_0) & t > t_0. \end{cases} \quad (6a)$$

Consider, for simplicity, the circumstance when $\varepsilon_T \geq \varepsilon_d$ during the entire creep stage. This corresponds to $\sigma_0 K_T(\sigma_0) \geq \varepsilon_d/D_0$, i.e. to $\sigma_0 \geq 44$ MPa (6.4 ksi).

In this case, the second parts of Equations (6a) and (7) yield

$$\begin{aligned} \varepsilon_r(\sigma_0, t) &= (1 - K_p)K_T(\sigma_0)(D_0 + D_1 t^n)\sigma_0 + K_p\varepsilon_d \\ &\quad - (1 - K_p)K_T(\sigma_0)\{[D_0 + D_1(t - t_0)^n]\sigma_0 + K_p\varepsilon_d\} \\ &\quad + \varepsilon_p(\sigma_0, t_0) \quad t > t_0. \\ &= (1 - K_p)K_T(\sigma_0)D_1[t^n - (t - t_0)^n]\sigma_0 \\ &\quad + K_p[K_T(\sigma_0)(D_0 + D_1 t_0^n)\sigma_0 - \varepsilon_d] \end{aligned} \quad (8)$$

Extensions to more general circumstances can be made in a straight forward manner.

A comparison between predicted and experimental values of recovery data are shown in Figure 16.

The presence of non-recoverable, permanent strain upon unloading is also observed in Figure 10.

Although ε_p was found to depend on both the amplitude and duration of applied stress, its magnitude is relatively small, usually less than 5 percent of the maximum strain. While this may be considered negligible for static creep tests, the influence of temperature, fluids or other loading histories on ε_p may alter its contribution. Therefore, the characterization and incorporation of ε_p is relevant to the ongoing work, which also involves repeated loadings.

4. Model verification tests

Model verification was attempted by conducting tests that differ in kind from the characterization experiments. The verification tests consisted of two-step creep and recovery runs. In the first step, the coupon was subjected to a stress σ_1 for a duration t_0 and allowed to recover for an extended period of time t_r ($t_r > 1000t_0$). Subsequently, in the second step, the coupon was reloaded to a stress σ_2 , which was maintained for the duration t_0 , then unloaded and again

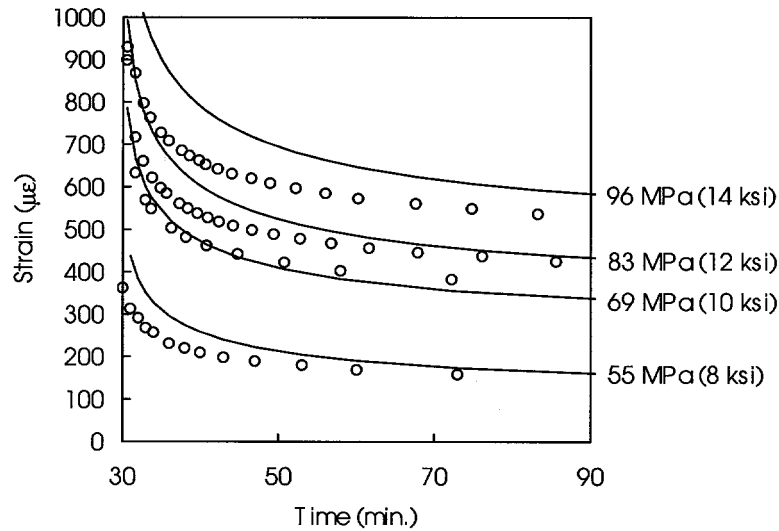


Figure 16. A comparison between the recorded (\circ) and predicted (—) strain recovery data upon accounting for the permanent strain ε_p .

allowed to recover for an extended period. Creep and recovery strains were recorded for the entire duration of the foregoing two-step test.

Predictions were based upon expressions (1)–(8), with the two additional hypotheses applying to the second step:

- (i) the total strain ε_T in Equation (3) corresponds to a compliance enhancement (i.e. modulus softening) caused by the highest stress employed in the two-step history.
- (ii) the permanent strain ε_p accumulates in a manner that is akin to that of a plastic strain of a strain-hardening material with linear unloading.

It should be noted that the creep and recovery data associated with the second stress σ_2 were recorded after both time and strain-gage readings were re-set at zero. Consequently, for $\sigma_2 > \sigma_1$, we have

$$\varepsilon(t) = \varepsilon_v(\sigma_2, t) + \varepsilon_p(\sigma_2, t) - \varepsilon_p(\sigma_1, t_0) \quad 0 \leq t < t_0 \quad (9)$$

and

$$\varepsilon(t) = \varepsilon_v(\sigma_2, t) - \varepsilon_v(\sigma_2, t - t_0) + \varepsilon_p(\sigma_2, t_0) - \varepsilon_p(\sigma_1, t_0) \quad t > t_0. \quad (10)$$

On the other hand, for $\sigma_2 < \sigma_1$ one obtains

$$\varepsilon(t) = [\varepsilon_v(\sigma_1, t) + \varepsilon_p(\sigma_1, t) - \varepsilon_p(\sigma_1, t_0)] \frac{\sigma_2}{\sigma_1} \quad 0 \leq t < t_0 \quad (11)$$

and

$$\varepsilon(t) = [\varepsilon_v(\sigma_1, t) - \varepsilon_v(\sigma_1, t - t_0)] \frac{\sigma_2}{\sigma_1} \quad t > t_0. \quad (12)$$

Expression (11) states that creep at $\sigma_2 < \sigma_1$ occurs in a coupon that was softened by the previous stress (σ_1), and since no new damage is presumed to arise, creep is linear in σ_2/σ_1 .

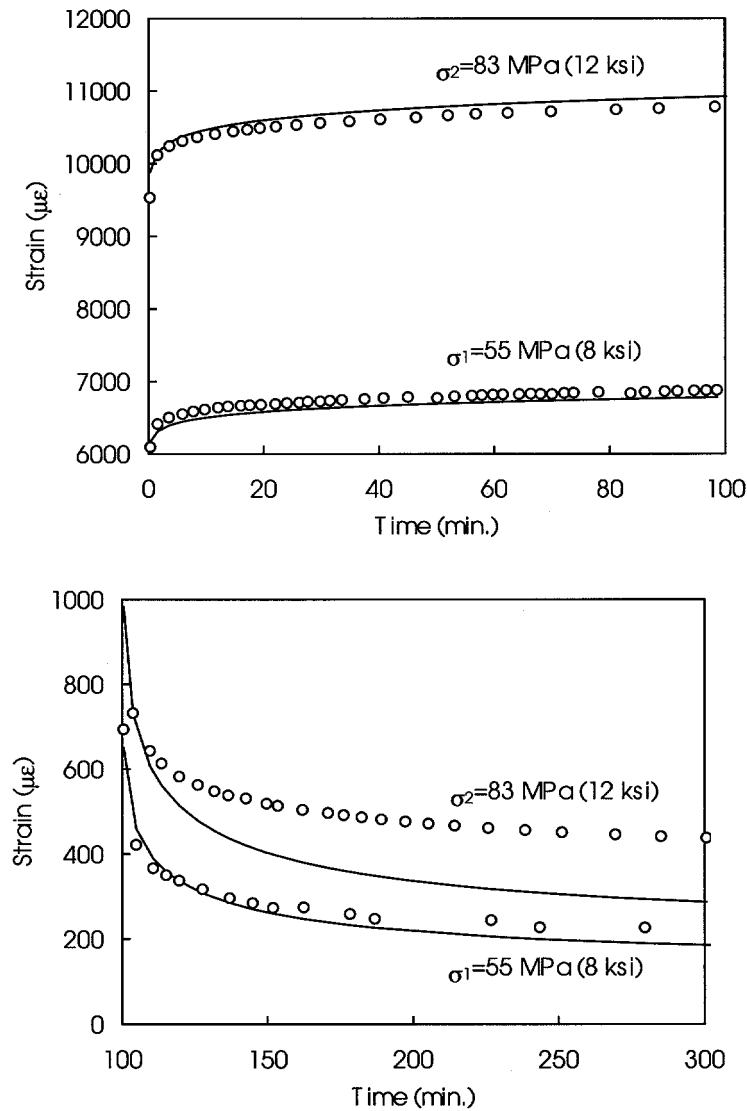


Figure 17. Comparison between the model (—) and experimental data (○) for the case of increasing stress ($\sigma_1 < \sigma_2$) for creep (top) and recovery (bottom). $D_0 = 9.0 \times 10^{-11} \text{ Pa}^{-1}$, D_1 and n are as reported in Figure 13.

Predictions based upon Equations (9) and (10) are compared against experimental data in Figure 17, where $\sigma_1 = 55 \text{ MPa (8 ksi)}$, $\sigma_2 = 83 \text{ MPa (12 ksi)}$ and $t_0 = 100 \text{ min}$. Similar comparisons, between data and predictions based upon Equations (11) and (12), are shown in Figure 18 for $\sigma_1 = 83 \text{ MPa (12 ksi)}$, $\sigma_2 = 55 \text{ MPa (8 ksi)}$ and $t_0 = 30 \text{ min}$. As in Figure 13, the time dependent portion of the prediction curves in Figures 17 and 18 derive from averaged properties (D_1 and n) while the instantaneous portion of the prediction curves (D_0) and the experimental curves correspond to individual specimens. Note the generally good agreements between data and predictions based upon Equations (9) through (12), in spite of the data scatter, although the recovery data do not appear to tend towards the values suggested

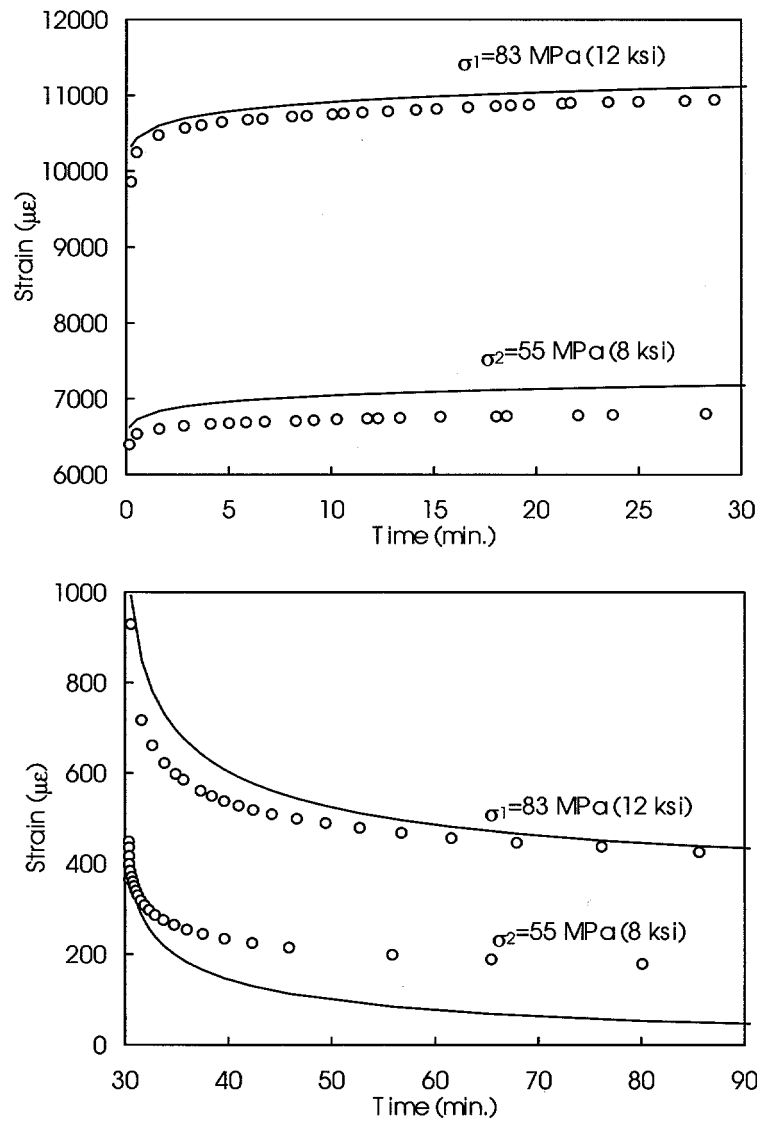


Figure 18. Comparison between the model (—) and experimental data (○) for the case of decreasing stress ($\sigma_1 > \sigma_2$) for creep (top) and recovery (bottom). $D_0 = 9.4 \times 10^{-11} \text{ Pa}^{-1}$, D_1 and n are as reported in Figure 13.

by Equations (10) and (12). The greater disparity in the predictions of recovery data is partly due to the presence of ϵ_p , which is highly random.

5. Concluding remarks

This article presented an assortment of microscopic observations and a systematic set of creep and recovery data regarding the response of swirl-mat composites. It has been noted that the mechanical response of these composites is extremely complex and involved aspects of viscoelasticity, damage due to profuse microcracking, and permanent strains upon load removal. The material exhibits substantial inhomogeneity, which is most likely due to the

rapidity of the SRIM process, as well as inherent randomness, which is attributable to the fiber architecture.

Obviously, the capability of any predictive model cannot exceed the inherent data scatter due to the above mentioned inhomogeneity and randomness of the material. Nevertheless, it has been shown that it was possible to distinguish between the foregoing causes by means of a sample-to-sample scaling procedure and thereby extricate information concerning the basic mechanisms that underlie the material response.

It was shown that creep could be expressed in power-law form, that damage could be quantified from data on modulus softening, and permanent strain could be correlated with the maximal strains that occurred during loading. Both damage and permanent strain develop beyond some threshold levels of stress and deformation, while at low stress levels the material's response accords with linear viscoelasticity.

The extension of the current work to more complex load histories would require information regarding the 'damage surface', akin to the yield surface in plasticity theory, which would relate the threshold value σ_d to previously applied stress levels. It is reasonable to expect that for essentially viscoelastic materials the above damage surface can be more appropriately related in strain space than in stress space. This suggestion is based on some recent findings (Corum, 1997) as well as on the realization that in viscoelastic materials fixed stresses correspond to increasing strains, while fixed strains correspond to diminishing stresses. Consequently, while maximal strains would be associated with the largest stresses, any stress envelope would be related to ever increasing strains. Consideration of strain space also provides some inherent normalization for composite materials with large scatter, since damage often depends more directly on strain than stress.

Acknowledgment

The support of the Durability of Lightweight Composite Structures Program at Oak Ridge National Laboratory is gratefully acknowledged. The Office of Transportation Materials, U.S. Department of Energy sponsored this research, under contract No. DE-AC05-84OR21400 with Lockheed Martin Energy Research Inc. The authors wish to express gratitude to Dr. Bill Simpson of ORNL for the *c*-scan image presented in Figure 2, Dr. Jack Lesko of VPI for providing the SPATE image shown in Figure 3, Mr. David Warren of ORNL for the SEM fracture image shown in Figure 5, and Dr. Mark Poliks of IBM for the confocal laser scan pictures shown in Figure 6.

References

- Abdel-Tawab, K. and Weitsman, Y.J. (1998). A Continuum model for viscoelasticity, damage and permanent deformation, with application to swirl-mat polymeric composites. *International Journal of Damage Mechanics*, **7**, pp. 351–380.
- Carley, E.P., Dockum, J.F. and Schell, P.L. (1990). Performing for liquid composite molding. *SAE Technical Paper Series* 900311, 115–132.
- Corum, J.M., McCoy, H.E., Ruggles, M.B. and Simpson, W.A. (1995). Durability of a continuous strand mat polymeric composite for automotive structural applications. *Proceedings of the Advanced Composites Conference and Exposition*. Dearborn Michigan, pp. 401–412.
- Corum, J.M. (1995). Durability of lightweight composite structures for automotive applications: Progress report for period ending September 30, Report # ORNL/TM-13176.
- Corum, J.M. (1997). Durability of lightweight composite structures for automotive applications. Progress report for period ending September 30, forthcoming.

- Henshaw, J.M., Doudican, J.C., Houston, D.Q. (1995). The effects of preload on the environmental resistance of glass-reinforced polyurethane. *Proceedings of the Advanced Composites Conference and Exposition*. Dearborn Michigan, pp. 413–423.
- Herring, H.M. (1997). Master's Thesis, University of Tennessee, forthcoming.
- Jerina, K.L., Schapery, R.A., Tung, R.W. and Sanders, B.A. (1982). Viscoelastic characterization of a random fiber composite material employing micromechanics. In *short fiber reinforced composite materials*, B.A. Sanders-Editor, *ASTM STP 772*, 225–250.
- Karger-Kocsis, J. (1990). Dynamic fracture mechanics of a RIM polyimide block copolymer reinforced with glass strand mat. *Polymer bulletin* **24**, 341–348.
- Karger-Kocsis, J. and Friedrich, K. (1991). Mechanical properties and failure behavior of glass fiber mat-reinforced bylon RIM composites. *Durability of Polymer Based Composite Systems for Structural Applications*. (Edited by Cardon, A.H and Verchery, G.). Elsevier Applied Science, pp. 158–168.
- Karger-Kocsis, J. (1992). Instrumented impact testing of a glass swirl mat-reinforced reaction injection-molded polyamide block copolymer (NBC). *Journal of Applied Polymer Science* **45**, 1595–1609.
- Karger-Kocsis, J. (1992). Fracture and failure behavior of glass fiber mat-reinforced structural nylon RIM composites. *Journal of Polymer Engineering*. **11**(1–2), 154–173.
- Karger-Kocsis, J., Czigan, T. (1993). Fracture behavior of glass-fibre mat-reinforces structural nylon RIM composites studied by microscopic and acoustic emission techniques. *Journal of Materials Science* **28**, 2438–2448.
- Lemaitre, J. and Chaboche, J.-L. (1990). *Mechanics of Solid Materials*. English Translation by B. Shrivastra, Cambridge University Press.
- Morii, T., Hamada, H., Maekawa, Z., Tanimoto, T., Hirano, T., Kiyosumi, K. and Tsujii, T. (1994). Weight changes of the fiber/matrix interface in GRP panels immersed in hot water. *Composites Science and Technology* **50**, 373–379.
- Otaigbe, J.U. and Harland, W.G. (1989). Impact fracture behavior of continuous glass fiber-reinforced nylon 6. *Journal of Applied Polymer Science* **33**, 77–89.
- Otaigbe, J.U. (1992). Effect of coupling agent and absorbed moisture on the tensile properties of a thermoplastic RIM composite. *Journal of Applied Polymer Science* **45**, 1213–1221.
- Peretz, D. and Weitsman, Y.J. (1982). Nonlinear viscoelastic characterization of FM-73 adhesive. *Journal of Rheology* **26**, 3; 245–261.
- Smith, L.V. and Weitsman, Y.J. (1998). *Inelastic Behavior of Randomly Reinforced Polymeric Composites Under Cyclic Loading*. *Mechanics Time-Dependent Materials*, Vol. 1, pp. 293–305.
- Stokes, V.K. (1990). Random glass mat reinforced thermoplastic composites. Parts I–IV, *Polymer Composites* **11**(1), 32–55, 342–367.
- Tomkinson-Walles, G.D. (1988). Performance of random glass mat reinforced thermoplastics. *Journal of Thermoplastic Composite Materials* **1**, 94–106.